

# Sodium and Potassium Storage Behaviour in AgNbO<sub>3</sub> Perovskite

Metin Orbay,<sup>[a]</sup> Abbas Khan,<sup>[b, c]</sup> Olivier Crosnier,<sup>[b, c]</sup> Thierry Brousse,<sup>[b, c]</sup> and Andrea Balducci<sup>[a]</sup>

In this work, we report on the investigation the perovskite-type AgNbO<sub>3</sub> as a model negative electrode for sodium and potassium systems. We demonstrated that during the initial discharge, regardless of the inserted cation, the material undergoes an activation mechanism that induces a crystalline-to-amorphous transition. This transition, in turn, leads to an

enhancement of the electrode capacity. At 5 A g<sup>-1</sup> sodium-ion AgNbO<sub>3</sub> and Potassium-ion AgNbO<sub>3</sub> display capacities of 81 mAh g<sup>-1</sup> and 60 mAh g<sup>-1</sup>, respectively. Furthermore, both electrodes display good cycling stability and efficiency over 350 cycles at 1 A g<sup>-1</sup>.

## Introduction

Given the increasing energy demands and the limitations in lithium supply, sodium and potassium ion chemistries are emerging as promising alternatives for rechargeable batteries.<sup>[1,2]</sup> Their appeal lies in several key factors: they are cost-effective, exhibit low redox potentials ( $-2.71$  V for Na<sup>+</sup>/Na and  $-2.94$  V for K<sup>+</sup>/K vs. SHE), and have a widespread, homogenous global distribution.<sup>[3]</sup> These characteristics present significant opportunities for developing sustainable and independent battery technologies. Nonetheless, moving from lithium-ion to sodium or potassium ions introduces new and unique challenges intrinsic to their chemistries. For instance, the varying ionic radii and charge densities of Na<sup>+</sup> (1.02 Å) and K<sup>+</sup> (1.38 Å) compared to Li<sup>+</sup> (0.76 Å) introduce new dynamics in solvent-ion stoke radius, kinetics (ion migration and diffusion) and thermodynamics (desolvation energy, ion-ion clustering) which dramatically affect the compatibility of many lithium-ion battery (LIB) materials with sodium-ion batteries (SIBs) and potassium-ion batteries (KIBs).<sup>[4,5]</sup> For instance, Graphite, as the state-of-the-art anode material for LIBs, cannot intercalate sodium ions without co-solvents, and shows substantial volume changes when operated with potassium-ions which could significantly increase parasitic reactions and capacity fading.<sup>[6,7]</sup>

Therefore, non-graphitic carbons such as hard carbon has been so far used as state-of-the-art anode for SIB.<sup>[8]</sup> Similar considerations can be made for alloying-type anodes such as metal anodes including Tin, Antimony or Bismuth<sup>[9]</sup> and conversion-type anodes.<sup>[10]</sup> These results are indicating that a direct transfer of the lithium-ion chemistry to SIBs and KIBs is not easy and in some cases, even not possible. Therefore, the behaviours of each active materials (and electrolytes) in lithium, sodium and potassium systems needs to be carefully investigated.

Recently, we have investigated in detail the storage mechanism of perovskite type AgNbO<sub>3</sub> as a model material for negative electrode in LIBs. We showed that during the lithium process at low potential (< 3 V vs. Li<sup>+</sup>/Li) an in-situ electrochemical exsolution process occurs, which greatly improves the capacity of this material.<sup>[11]</sup> This improvement was found to originate from the creation of A-site silver vacancies enhancing the material's active niobium redox sites, which significantly enhances rate performances as well as the specific capacity of the material in comparison to the pristine AgNbO<sub>3</sub>.<sup>[12]</sup> Moreover, we observed a crystalline to amorphous transition which does not affect electrochemical performance, while exsolved nano-silver particles from the perovskite were shown to enhance particle percolation.<sup>[13,14]</sup> To the best of our knowledge, the electrochemical behaviour of AgNbO<sub>3</sub> in sodium and potassium systems has not been studied in detail so far. In this study we want to address this point and investigate in detail the sodium and potassium insertion in this model electrode, with the aim of understanding the similarities and differences with the previously studied lithium insertion.

[a] M. Orbay, A. Balducci  
Friedrich-Schiller-University Jena, Institute of Technical Chemistry and Environmental Chemistry and Center for Energy and Environmental Chemistry, Jena, Germany

[b] A. Khan, O. Crosnier, T. Brousse  
Nantes Université, CNRS, Institut des Matériaux de Nantes Jean Rouxel, IMN, F-44000 Nantes, France

[c] A. Khan, O. Crosnier, T. Brousse  
Réseau sur le Stockage Electrochimique de l'Energie (RS2E), CNRS FR 3459, 80039 Amiens, France

 Supporting information for this article is available on the WWW under <https://doi.org/10.1002/batt.202400602>

 © 2024 The Authors. Batteries & Supercaps published by Wiley-VCH GmbH. This is an open access article under the terms of the Creative Commons Attribution Non-Commercial License, which permits use, distribution and reproduction in any medium, provided the original work is properly cited and is not used for commercial purposes.

## Experimental Section

### Material Synthesis

AgNbO<sub>3</sub> perovskites were synthesized using a polymerization-based sol-gel method known as polyacrylamide synthesis. Metal precursors, silver nitrate (AgNO<sub>3</sub>, Alfa Aesar, 99.9%) and niobium oxalate hydrate (C<sub>10</sub>H<sub>5</sub>NbO<sub>20</sub>·xH<sub>2</sub>O, Alfa Aesar) were dissolved in ethylene glycol (Alfa Aesar) while stirring at 25 °C. The Ag/Nb precursor ratio was kept 1. Citric acid (HOC(CH<sub>2</sub>CO<sub>2</sub>H)<sub>2</sub>, Alfa Aesar, 99 + %) in 1.5:1

cation molar ratio was added as complexing agent, and the mixture was stirred until a transparent solution was achieved. In next step, acrylamide monomers (Alfa Aesar) and N,N'-methylene-bisacrylamide (Alfa Aesar) cross-linkers were introduced into the solution at a cation molar ratio of 9:1. Adding appropriate amount of polymerization initiator Ammonium persulfate (Sigma Aldrich, ≥ 99.99%) and hydrogen peroxide (30% w/w H<sub>2</sub>O<sub>2</sub> in H<sub>2</sub>O, Sigma Aldrich) leads to formation of wet polymeric gel within 20 minutes leading to the development of a 3D network of interconnected loops. Wet gel was subsequently converted to xerogel by heating in an oven under 250 °C. The final AgNbO<sub>3</sub> materials were obtained by grinding the xerogel and annealing it at 650 °C in air for 12 hours (S1). The powder is made of round-shaped grains with an average grain size of about 150 nm. The BET surface area measured by N<sub>2</sub> adsorption is 6.7 m<sup>2</sup> g<sup>-1</sup>. By modelizing spherical grains in the powder and taking into account the theoretical density of AgNbO<sub>3</sub> (6.784 g cm<sup>-3</sup>), the diameter should be 132 nm which is in good agreement with the mean diameter measured from SEM images. Thus, the porosity of the powder is mainly coming by the piling up of individual bulk particles of AgNbO<sub>3</sub>.

### Electrochemical Measurements and Electrode Preparation

Slurries containing 85% wt. active material (AgNbO<sub>3</sub>), 10% wt. conducting agent (Imerys Super C65) and 5% wt. binder (Walocel sodium carboxymethyl cellulose CMC2000) were prepared and cast onto copper foil via doctor blading. AgNbO<sub>3</sub> electrode mass loadings ranged from 1.2 to 2.5 mg cm<sup>-2</sup>. Propylene Carbonate (PC) anhydrous 99.7% was purchased from Sigma Aldrich. Sodium bis(fluorosulfonyl)imide (NaFSI) (99.9%) and Potassium bis(fluorosulfonyl)imide (KFSI) (99.9%) were purchased from Solvionic and used to prepare the electrolytes at room temperature. Swagelok-type® cells were used to study the electrochemical performance of AgNbO<sub>3</sub> electrodes in a three-electrode cell setup. The working electrode (WE) was AgNbO<sub>3</sub>, whereas the reference electrode (Ref) and the counter electrode (CE) were Sodium or Potassium Metal. Biologic VMP-3 and MPG-200 potentiostats were used for all electrochemical studies. The total area of all electrodes was 1.13 cm<sup>2</sup>.

Diffusion coefficient of AgNbO<sub>3</sub> electrodes in the investigated systems were measured using galvanostatic intermittent titration technique (GITT) using the method described by W. Weppner,<sup>[15]</sup> according to the following equation:

$$D_i = \frac{4}{\pi\tau} \left( \frac{m_A V_M}{M_A S} \right)^2 \left( \frac{\Delta E_{eq}}{\Delta E_{relax}} \right)^2, \quad (\tau \ll \frac{l^2}{D_i})$$

Where  $\tau$  is the duration of the current pulse,  $M_A$  is the molar mass of AgNbO<sub>3</sub>,  $m_A$  is the mass of the active material,  $L$  is the thickness of the active material and  $S$  is the surface area of the electrode. The assumption of negligible volume change within the sample allows these parameters to be considered constant.  $\Delta E_{eq}$  and  $\Delta E_{relax}$  represent the differences between the equilibrium potential and the potential at the end of a current pulse and after the relaxation period of the cell, respectively. Cell assembly and electrolyte preparation were carried out in an argon-filled glovebox (O<sub>2</sub> and H<sub>2</sub>O < 1 ppm).

### Physical Characterizations

X-ray diffraction measurements were conducted using Burker D2-PHASER with Cu-K<sub>α1</sub>-K<sub>α2</sub> ( $\lambda = 1.54060 \text{ \AA}$ ,  $1.54443 \text{ \AA}$ ) using acceleration voltage of 30 kV at 10 mA. XRD data was recorded using 2θ range of 3° to 80°.

Operando Raman measurement was performed using a Renishaw InVia confocal Raman microscope, equipped with a 532 nm laser operated with a power of 2.5 mW, which was coupled with a biologic SP-150 potentiostat. The operando cell is supplied by ELCELL ECC-Opto-Std equipped with Raman transparent sapphire window. After assembly, the cell was rested for 24 h at OCV.

### Results

In our previous work, we demonstrated that even with a 100% occupancy of the A site by Ag<sup>+</sup> cations in the AgNbO<sub>3</sub> structure, it is possible to induce a silver exsolution process electrochemically.<sup>[11]</sup> This process promotes the formation of open channels for cation diffusion and niobium redox site activation, significantly enhancing the capacity of the material at low potentials.<sup>[16]</sup> To verify whether this exsolution mechanism also occurs when sodium and potassium cations are utilized, AgNbO<sub>3</sub> electrodes were cycled in sodium and potassium-based electrolytes in half cell configuration against sodium and potassium metal, respectively.

Figure 1a and c depict the galvanostatic charge discharge profiles of AgNbO<sub>3</sub>. To showcase the underlying activation step, the electrodes were cycled initially at a potential above the activation potential limit (at 0.6 V vs Na<sup>+</sup>/Na and K<sup>+</sup>/K) and, subsequently, below this limit (at 0.01 V vs Na<sup>+</sup>/Na and K<sup>+</sup>/K). As shown, when a 0.6 V cutoff potential is applied, AgNbO<sub>3</sub> provides negligible capacity of 20 mAh g<sup>-1</sup> and 8 mAh g<sup>-1</sup> for sodium and potassium-ions, respectively. This low capacity is primarily due to a capacitive storage behavior, as shown in Figure 1b and d. When the electrodes are cycled below the activation limit value, which can be seen in a plateau at threshold potentials of 0.19 V for sodium and 0.13 V for potassium, the electrochemical behavior of the electrodes changes significantly. Below this value, the capacity increases up to 350 mAh g<sup>-1</sup> and 325 mAh g<sup>-1</sup> during the first discharge for sodium and potassium respectively. Although these capacities could not be fully recovered upon subsequent cycles, they reach stable values of 145 mAh g<sup>-1</sup> and 126 mAh g<sup>-1</sup>, and these values are maintained during subsequent cycles.

After the activation, the AgNbO<sub>3</sub> electrodes exhibit an electrochemical response characterized by a broad peak current below 2 V during reduction sweep, indicative of fast niobium redox processes (Figures 1b and d). It is also noteworthy that, in sodium and potassium systems, Na–Ag and K–Ag alloying cannot be clearly identified, unlike the Li–Ag alloying seen in the AgNbO<sub>3</sub> system. While the observed plateaus could imply an irreversible alloying reaction, previous studies on the Ag–K and Ag–Na phase diagrams suggest this is unlikely due to the extremely low solubility of these alkali metals in Ag compared to Li<sup>[17,18]</sup> which is much more favorable. The irreversibility of the plateau suggests that its very unlikely that this process involves any metastable Ag–Na or Ag–K phase. Therefore, the observed single-phase transformation is most likely a result of material restructuring, that is, amorphous transformation. Consequently, these findings indicate that the activation mechanism of

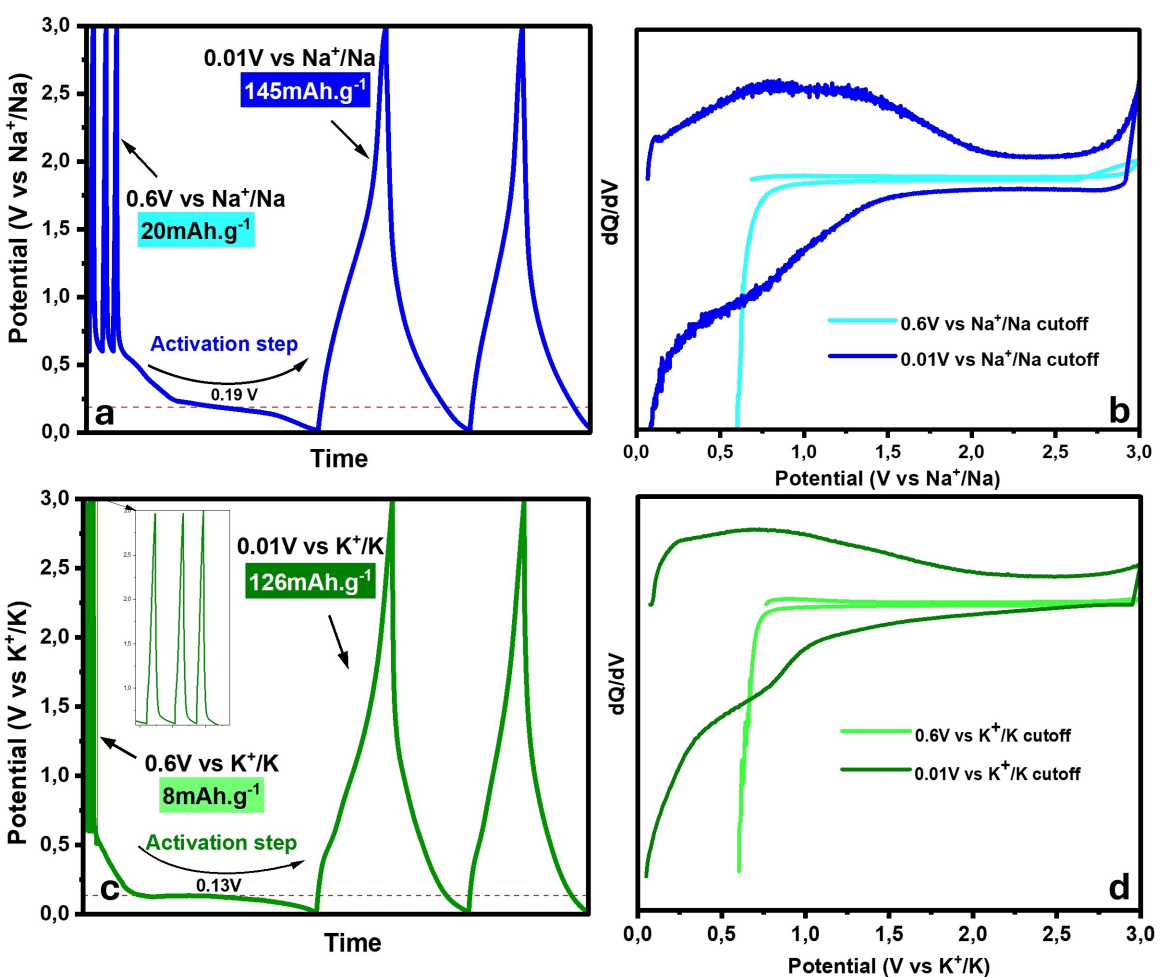


**Figure 1.** (a) and (c) Potential profiles of AgNbO<sub>3</sub> electrode in sodium and potassium systems before and after the electrochemical activation of the electrodes. (b) and (d) comparison of Differential capacity response of AgNbO<sub>3</sub> in Sodium and Potassium at 0.6 V vs 0.01 V.

AgNbO<sub>3</sub> occurs with sodium and potassium as well, though the electrochemical behavior differs from that seen with lithium.

Figure 2a compares the X-ray diffraction patterns of pristine AgNbO<sub>3</sub>, with (ex-situ) AgNbO<sub>3</sub> electrodes cycled in a half cell configuration against sodium and potassium metal. The previous refinement of the pristine sample confirms the formation of an orthorhombic perovskite phase belonging to the Pbcm space group (Table S1). This is consistent with previous findings<sup>[19]</sup> and exhibit the targeted morphology (S2), which served as our baseline. However, the X-ray diffraction pattern of cycled ex-situ electrodes in potassium and sodium systems show a significant change in the crystallinity of AgNbO<sub>3</sub> in contrast to the pristine electrode, losing all defined phase peaks after electrochemical measurements. Nevertheless, complete amorphization of the material may not be achieved, and some pristine phase could still remain. *In situ* X-ray diffraction indicated that this phenomenon is associated to a crystalline-to-amorphous transformation within the material as demonstrated to exist in Lithium AgNbO<sub>3</sub> and other perovskite oxides,<sup>[11,20]</sup> indicating that this process also occurs for sodium and potassium-based cation systems. To further understand this mechanism, in-operando Raman spectroscopy have been

carried out and two vibrational modes: A<sub>1g</sub>(ν<sub>1</sub>) and F<sub>2g</sub>(ν<sub>5</sub>) describing the double-degenerate symmetric O–Nb stretching and a triple degenerate symmetric O–Nb bending in the NbO<sub>6</sub> octahedral cage, respectively, have been investigated.<sup>[21]</sup> These vibration mode have been selected because their modification, caused by the abovementioned amorphous transformation, should be observable in the Raman spectra.<sup>[22,23]</sup> As shown in Figure 2b and c the ν<sub>5</sub> vibration, which relates to the Nb<sup>5+</sup> cation displacement and NbO<sub>6</sub> octahedra tilting, is found to become weakened in intensity as more reductive potentials are reached. Similarly, ν<sub>1</sub> vibration also experiences weakened intensity with the applied potential. These results highlight that changes in the structural integrity of the material in potassium and sodium systems occur as the material is discharged to reductive potentials, leading to a structurally altered AgNbO<sub>3</sub>. This finding aligns with previous results for lithium based perovskites<sup>[11,20,24]</sup> and further underscores that the structural amorphous transformation observed in AgNbO<sub>3</sub> is also observed in Na and K based systems.

The comparison of the electrochemical performance of AgNbO<sub>3</sub> in sodium and potassium systems is presented in Figure 3. For benchmarking purposes, the performance of hard

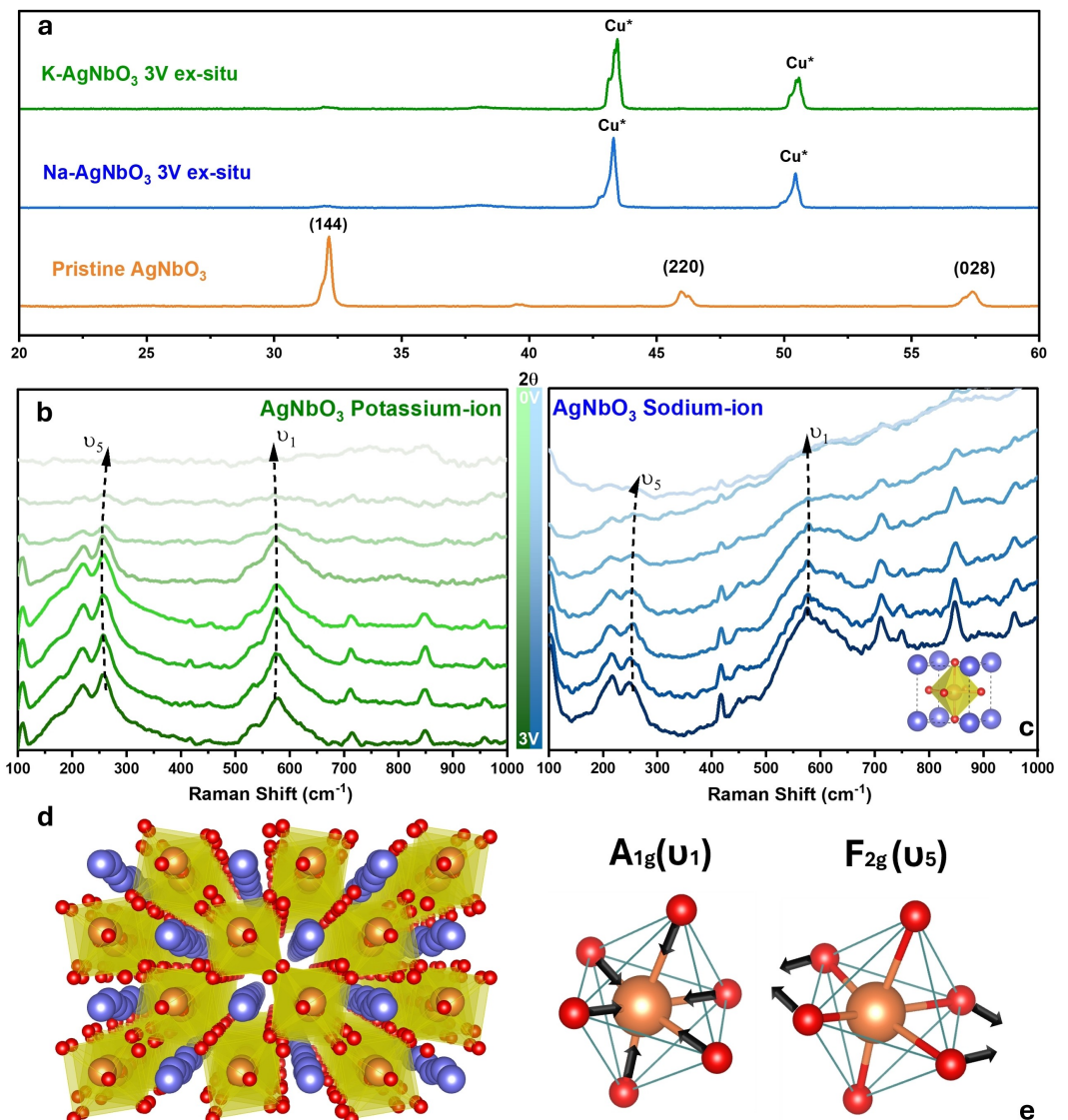


**Figure 2.** (a) Normalized ex-situ X-ray diffraction patterns of Pristine AgNbO<sub>3</sub>, Na-AgNbO<sub>3</sub> and K-AgNbO<sub>3</sub> electrodes stopped and analysed at 3 V vs M<sup>+</sup>/M<sup>-</sup> cycled in 1 M NaFSI and 1 M KFSI in PC (0.01–3 V). (b) and (c) Operando Raman spectroscopy of Na-AgNbO<sub>3</sub> and K-AgNbO<sub>3</sub> discharged from 3 to 0.01 V. (d) face centered schematic representation of AgNbO<sub>3</sub> perovskite structure, showcasing the tunnels filled with cage centered silver atoms (colored in blue) surrounded by the [NbO<sub>6</sub>] octahedra. (e) schematic representation of [NbO<sub>6</sub>] octahedra with the followed A<sub>1g</sub>(v<sub>1</sub>) stretching and F<sub>2g</sub>(v<sub>5</sub>) bending vibrations.

carbon in a sodium with similar mass loading and electrolyte volume saturation to AgNbO<sub>3</sub> electrodes can be found in supplementary work (see S6). The first coulombic efficiency of K-AgNbO<sub>3</sub> Na-AgNbO<sub>3</sub> is considered low (60%) due to the activation processes, however, HC presents similar limitations in terms of first cycle efficiency (S5). Moreover, as shown in Figure 3a, Na-AgNbO<sub>3</sub> and K-AgNbO<sub>3</sub> present a slightly slopy discharge profile at around 1 V vs Na<sup>+</sup>/Na and 0.9 V vs K<sup>+</sup>/K. The sloping nature of the charge-discharge curves indicates a prominent pseudocapacitive process, a behaviour that was not as clearly observed in lithium-based systems.<sup>[11]</sup> This could be due additional surface redox processes in potassium and sodium electrolytes as their ionic Radii and solvation energies differ from the latter in organic electrolytes,<sup>[25]</sup> which could also explain the good performance at high current densities. As shown in Figure 3b, Na-AgNbO<sub>3</sub> achieves 145, 127, 117, 108, 98,

and 81 mAh g<sup>-1</sup> at 0.1, 0.2, 0.5, 1, 2, and 5 Ag<sup>-1</sup>, respectively. Similarly, in potassium system, K-AgNbO<sub>3</sub> delivers 126, 103, 88, 79, 71, and 60 mAh g<sup>-1</sup> at 0.1, 0.2, 0.5, 1, 2, and 5 Ag<sup>-1</sup>, respectively. These capacity values are promising, especially at higher current densities, and are comparable to or better than other potassium-based anodic materials reported in literature.<sup>[26–29]</sup> It is also interesting to notice that the rate capability of Na-AgNbO<sub>3</sub> is better than that of hard carbon anode cycled in similar conditions (S6). The estimated diffusion coefficient for sodium and potassium in AgNbO<sub>3</sub> is in the order of ~10<sup>-10</sup>–10<sup>-11</sup> cm<sup>2</sup>s<sup>-1</sup> at 298 K (see GITT measurement in S7), which is a value comparable to previously reported high-rate anode materials such as Na<sub>2</sub>Ti<sub>3</sub>O<sub>7</sub>, T-Nb<sub>2</sub>O<sub>5</sub>, Li<sub>4</sub>Ti<sub>5</sub>O<sub>12</sub> and NaVO<sub>3</sub> in sodium and potassium chemistries (see comparative table in S2) indicating fast diffusion processes.<sup>[30–33]</sup> Figure 3c compares the long-term cycling stability of AgNbO<sub>3</sub> in both sodium and

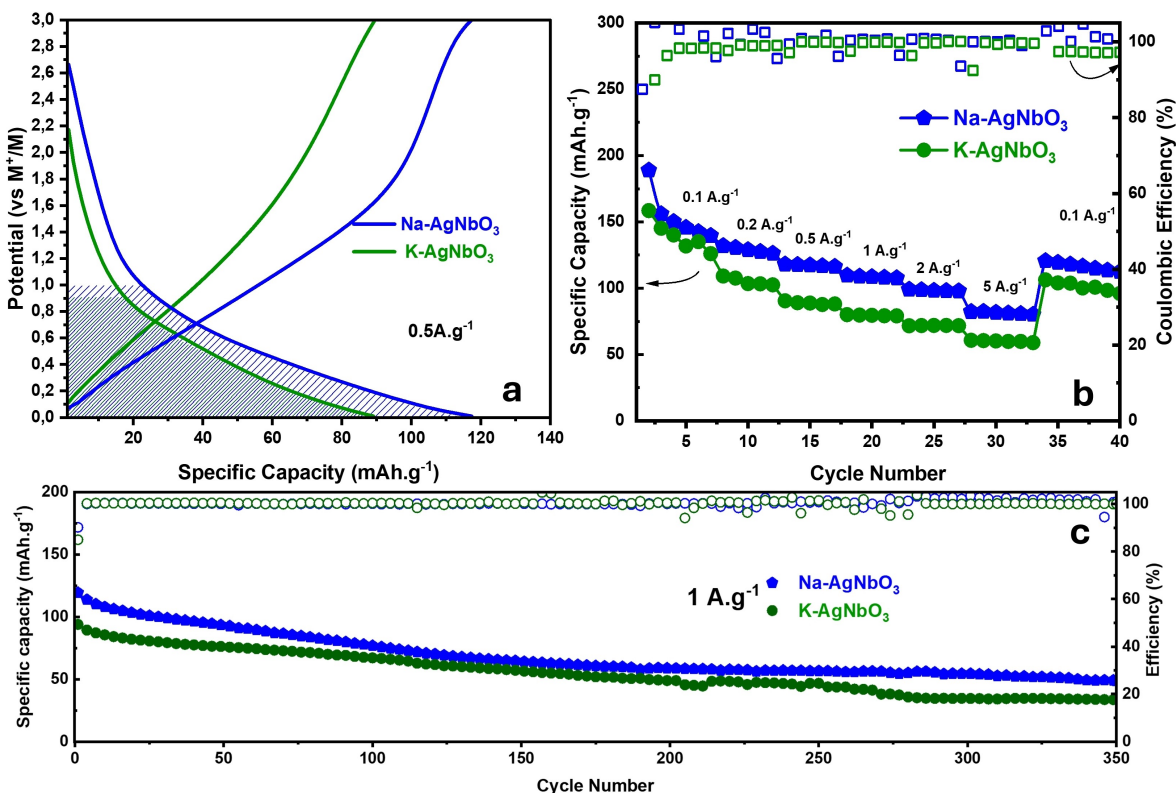


**Figure 3.** (a) Charge-discharge profiles of Na-AgNbO<sub>3</sub> and K-AgNbO<sub>3</sub> at 0.5 A g<sup>-1</sup>. Dashed area represents the bulk capacity potential onset. (b) Rate test of Na-AgNbO<sub>3</sub> and K-AgNbO<sub>3</sub> from 0.1 to 5 A g<sup>-1</sup>. (c) Long term capacity retention displayed by Na-AgNbO<sub>3</sub> and K-AgNbO<sub>3</sub> 1 A g<sup>-1</sup>.

potassium systems at 1 A g<sup>-1</sup> during 350 cycles. As shown, Na-AgNbO<sub>3</sub> display good long-term stability and coulombic efficiency, and the electrode was able to retain 73% of its initial capacity after 350 cycles. K-AgNbO<sub>3</sub> displays a similar stability retaining 74% of its initial capacity at the end of the cycling process. These results are indicating that both electrodes can be successfully cycled over an extended potential range (0.01–3 V vs Na<sup>+</sup>/Na or K<sup>+</sup>/K).

One remarkable feature about AgNbO<sub>3</sub> is the peculiar shape of the GCD and CV plots both in Na<sup>+</sup> and K<sup>+</sup> based electrolytes which are neither battery type nor capacitive/pseudocapacitive but rather seem to be a mixture of both. These shapes were analysed using the facilities provided by the work of Deebasok et al.<sup>[34]</sup> According to the shape, the software proposed a pseudocapacitive trend close to 96% whatever the scan rate used for the cyclic voltammetry experiences. However, it must be noted that such analysis is only based on the shape of the related CV and more in-depth analysis of the data are required to differentiate the phenomena at play. To further elucidate the charge storage mechanisms of AgNbO<sub>3</sub> in the presence of K<sup>+</sup> and Na<sup>+</sup> cations, cyclic voltammetry at different sweep rates have been carried out. This approach allows us to differentiate between diffusion-controlled faradaic processes and (pseudo)capacitive charge storage processes.<sup>[35,36]</sup> To quantitatively determine the (pseudo)capacitive and diffusion-dominated contributions to the total current response of AgNbO<sub>3</sub> in K<sup>+</sup> and Na<sup>+</sup> systems, the current response *i* at a given potential *V* can be separated into capacitive ( $k_1v$ ) and diffusion-

dominated ( $k_2v^{1/2}$ ) processes. This relationship is expressed by the equation:

$$i(V) = k_1v + k_2v^{1/2}$$

where  $k_1$  and  $k_2$  are constants,  $v$  is the scan rate, and  $i(V)$  is the measured total current response at a fixed potential  $V$ . To determine the values of  $k_1$  and  $k_2$ , one can plot  $\frac{i(V)}{v^{1/2}}$  against  $v^{1/2}$ .

From this plot, the slope provides the  $k_1$ -value, while the intercept represents the  $k_2$ -value. Although there are some limitations to the use of such method, especially with regards to the equivalent series resistance of the electrodes, the obtained results were coherent enough to be further analysed. Figure 4 presents the results of this analysis for K-AgNbO<sub>3</sub> and Na-AgNbO<sub>3</sub> from a scan rate of 0.1 to 2 mV s<sup>-1</sup>. As shown in Figure 4b and c, the pseudocapacitive contribution to the current output is calculated as 30% in Na-AgNbO<sub>3</sub> and 27% in K-AgNbO<sub>3</sub>. This indicates that at low current densities, the majority of the capacity is diffusion controlled. However, as expected, the capacitive contribution gradually increases with higher sweep rates, reaching 62% and 66% of the total current output at 2 mV s<sup>-1</sup>. This increase in capacitive contribution at higher sweep rates explains the good rate performance observed for AgNbO<sub>3</sub>, due to the dominance of fast redox processes observed at current densities above 1 A g<sup>-1</sup>, probably related to surface redox reactions.

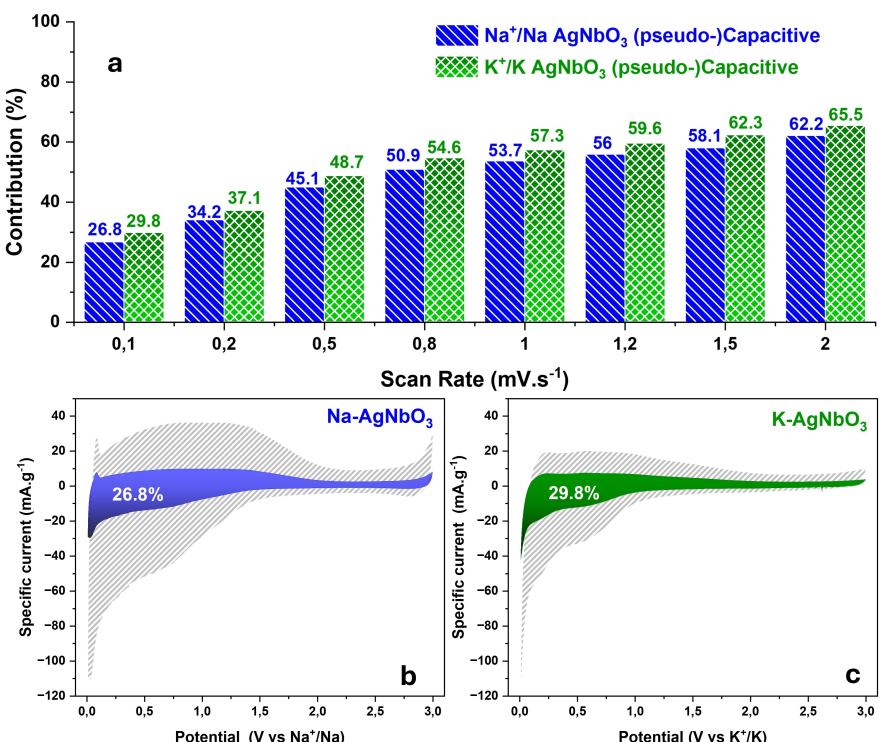


**Figure 4.** (a) Analysis of the relative contributions of diffusion-controlled and (pseudo)capacitive processes to the total charge storage for Na-AgNbO<sub>3</sub> (Blue) and K-AgNbO<sub>3</sub> (Green), determined through cyclic voltammetry at different sweep rates. (b) and (c) provide illustrative examples of the (pseudo)capacitive contributions for Na-AgNbO<sub>3</sub> (Blue) and K-AgNbO<sub>3</sub> (Green).

## Conclusions

In this work, we analysed AgNbO<sub>3</sub>-type perovskite as a model negative electrode for sodium and potassium systems. We observed that the electrodes undergo an activation mechanism similar to that of lithium-based AgNbO<sub>3</sub>, exhibiting an activation barrier potential of 0.19 and 0.13 V towards Na<sup>+</sup>/Na and K<sup>+</sup>/K respectively. Once electrochemical activation occurs, the capacity of AgNbO<sub>3</sub> increases significantly and structural changes are observed, which were studied using ex-situ X-ray spectroscopy and operando Raman spectroscopy. We also showed that the process is dependent on surface redox processes and that the performance is not significantly affected by the application of higher current densities, reaching 81 mAh g<sup>-1</sup> and 60 mAh g<sup>-1</sup> at 5 Ag<sup>-1</sup> for sodium-ion intercalated AgNbO<sub>3</sub> and potassium-ion intercalated AgNbO<sub>3</sub> respectively. Furthermore, good stability and efficiency were demonstrated for the sodium and potassium systems during 350 cycles at 1 Ag<sup>-1</sup>. This research paves the way for investigating the properties of exsolved ABO<sub>3</sub>-type perovskites and lays the groundwork for their application as tailored materials for high-power, wide voltage range (up to 0.01 V) sodium and potassium-based anode material applications.

## Acknowledgements

The authors wish to thank the Friedrich-Schiller University, Metin Orbay and Abbas Khan as a part of the DESTINY PhD

programme (Doctorate programme on Emerging battery Storage Technologies INspiring Young scientists) acknowledges funding from the European Union's Horizon 2020 research and innovation programme under the Marie Skłodowska-Curie Actions Cofund Grant Agreement No: 945357. The authors would like to acknowledge Labex STORE-EX (ANR-10-LABX-76-01) and PEPR Batteries (France 2030), project HIPOHYBAT, for financial support. Open Access funding enabled and organized by Projekt DEAL.

## Conflict of Interests

The authors declare no conflict of interest.

## Data Availability Statement

The data that support the findings of this study are available from the corresponding author upon reasonable request.

- [1] N. Yabuuchi, K. Kubota, M. Dahbi, S. Komaba, *Chem. Rev.* **2014**, *114*, 11636.
- [2] X. Min, J. Xiao, M. Fang, Wei (Alex) Wang, Y. Zhao, Y. Liu, A. M. Abdelkader, K. Xi, R. Vasant Kumar, Z. Huang, *Energy Environ. Sci.* **2021**, *14*, 2186.
- [3] C. Vaalma, D. Buchholz, M. Weil, S. Passerini, *Nat. Rev. Mater.* **2018**, *3*, 1.
- [4] R. Rajagopalan, Y. Tang, X. Ji, C. Jia, H. Wang, *Adv. Funct. Mater.* **2020**, *30*, 1909486.
- [5] M. Sha, L. Liu, H. Zhao, Y. Lei, *Carbon Energy* **2020**, *2*, 350.

- [6] Y. Li, Y. Lu, P. Adelhelm, M.-M. Titirici, Y.-S. Hu, *Chem. Soc. Rev.* **2019**, *48*, 4655.
- [7] B. Jache, J. Oliver Binder, T. Abe, P. Adelhelm, *Phys. Chem. Chem. Phys.* **2016**, *18*, 14299.
- [8] J. L. Gómez-Urbano, C. Leibing, M. Jauregui, S. Darlami-Magar, D. Saurel, D. Carriazo, A. Balducci, *Batteries & Supercaps* **2023**, *6*, e202200508.
- [9] K. Song, C. Liu, L. Mi, S. Chou, W. Chen, C. Shen, *Small* **2021**, *17*, 1903194.
- [10] S. Fang, D. Bresser, S. Passerini, *Adv. Energy Mater.* **2020**, *10*, 1902485.
- [11] A. Khan, M. Orbay, N. Dupré, E. Gautron, E. L. Calvez, O. Crosnier, A. Balducci, T. Brousse, *Energy Storage Mater.* **2024**, *70*, 103431.
- [12] Y.-F. Sun, Y.-Q. Zhang, J. Chen, J.-H. Li, Y.-T. Zhu, Y.-M. Zeng, B. S. Amirkhiz, J. Li, B. Hua, J.-L. Luo, *Nano Lett.* **2016**, *16*, 5303.
- [13] O. Kwon, S. Joo, S. Choi, S. Sengodan, G. Kim, *J. Phys. Energy* **2020**, *2*, 032001.
- [14] D. Neagu, G. Tsekouras, D. N. Miller, H. Ménard, J. T. S. Irvine, *Nat. Chem.* **2013**, *5*, 916.
- [15] W. Weppner, R. A. Huggins, *J. Electrochem. Soc.* **1977**, *124*, 1569.
- [16] B.-W. Zhang, M.-N. Zhu, M.-R. Gao, X. Xi, N. Duan, Z. Chen, R.-F. Feng, H. Zeng, J.-L. Luo, *Nat. Commun.* **2022**, *13*, 4618.
- [17] A. D. Pelton, *Bull. Alloy Phase Diagrams* **1986**, *7*, 133.
- [18] A. D. Pelton, *Bull. Alloy Phase Diagrams* **1986**, *7*, 223.
- [19] P. Sciau, A. Kania, B. Dkhil, E. Suard, A. Ratuszna, *J. Phys. Condens. Matter* **2004**, *16*, 2795.
- [20] X. Li, Z. Lin, N. Jin, L. Sun, X. Yang, Y. Liu, *Adv. Funct. Mater.* **2023**, *33*, 2214667.
- [21] M. K. Niranjani, K. G. Prasad, S. Asthana, S. Rayaprol, V. Siruguri, *J. Phys. D* **2015**, *48*, 215303.
- [22] K. Dai, A. Cui, Y. Ye, K. Jiang, J. Zhang, Y. Li, G. Wang, X. Dong, Z. Hu, J. Chu, *Phys. Rev. B* **2021**, *104*, 174104.
- [23] A. Kania, K. Roleder, G. E. Kugel, M. D. Fontana, *J. Phys. C* **1986**, *19*, 9.
- [24] W. Hou, Y. Yang, L. Fang, Y. Mao, W. Sun, Y. Bai, K. Sun, Z. Wang, *Chem. Eng. J.* **2021**, *409*, 128079.
- [25] M. Okoshi, Y. Yamada, S. Komaba, A. Yamada, H. Nakai, *J. Electrochem. Soc.* **2016**, *164*, A54.
- [26] X. Min, J. Xiao, M. Fang, Wei (Alex) Wang, Y. Zhao, Y. Liu, A. M. Abdelkader, K. Xi, R. Vasant Kumar, Z. Huang, *Energy Environ. Sci.* **2021**, *14*, 2186.
- [27] Y. Ma, Y. Ma, H. Euchner, X. Liu, H. Zhang, B. Qin, D. Geiger, J. Biskupek, A. Carlsson, U. Kaiser, A. Groß, S. Indris, S. Passerini, D. Bresser, *ACS Energy Lett.* **2021**, *6*, 915.
- [28] S. Wang, F. Chen, L. Zhang, Y. Li, N. Ren, K. Cao, J. Xiao, C. Chen, *Nanoscale* **2022**, *14*, 5347.
- [29] X. Niu, Y. Zhang, L. Tan, Z. Yang, J. Yang, T. Liu, L. Zeng, Y. Zhu, L. Guo, *Energy Storage Mater.* **2019**, *22*, 160.
- [30] G. Ali, M. Islam, H.-G. Jung, K.-W. Nam, K. Y. Chung, *ACS Appl. Mater. Interfaces* **2018**, *10*, 18717.
- [31] H. J. Kim, J. H. Jo, J. U. Choi, N. Voronina, D. Ahn, T.-Y. Jeon, H. Yashiro, Y. Aniskevich, G. Ragoisha, E. Streltsov, S.-T. Myung, *Energy Storage Mater.* **2021**, *40*, 197.
- [32] A. Rudola, K. Saravanan, C. W. Mason, P. Balaya, *J. Mater. Chem. A* **2013**, *1*, 2653.
- [33] G. Chen, J. Chen, S. Zhao, G. He, T. S. Miller, *ACS Appl. Mater. Interfaces* **2023**, *15*, 16664.
- [34] S. Deebansok, J. Deng, E. Le Calvez, Y. Zhu, O. Crosnier, T. Brousse, O. Fontaine, *Nat. Commun.* **2024**, *15*, 1133.
- [35] J. Wang, J. Polleux, J. Lim, B. Dunn, *J. Phys. Chem. C* **2007**, *111*, 14925.
- [36] R. Cheng, T. Hu, H. Zhang, C. Wang, M. Hu, J. Yang, C. Cui, T. Guang, C. Li, C. Shi, P. Hou, X. Wang, *J. Phys. Chem. C* **2019**, *123*, 1099.

Manuscript received: September 12, 2024

Revised manuscript received: October 11, 2024

Accepted manuscript online: October 12, 2024

Version of record online: November 9, 2024